Nano Research

ISSN 1998-0124 CN 11-5974/O4
https://doi.org/10.26599/NR.2026.94908748

Research Article

High-performance quantum dots enabled by supplementary passivation using ethoxydiphenylphosphine

Hao Luo[1], Zhijiao Huang[1], Bo-Yi Deng[1], Chenyu Zhang[1], Yang Liu[1], Ke Peng[2], Rui Long[1], Xiangzhen Deng[1], Daoli Zhang[1], Liang Gao[3], Yanwei Wen[2], Jianbing Zhang[1](✉), Jiang Tang[3]

[1] School of Integrated Circuits, Huazhong University of Science and Technology, Wuhan 430074, China

[2] School of Materials Science and Engineering, Huazhong University of Science and Technology, Wuhan 430074, China

[3] Wuhan National Laboratory for Optoelectronics, Huazhong University of Science and Technology, Wuhan 430074, China

Nano Res., **Just Accepted Manuscript** • https://doi.org/10.26599/NR.2026.94908748

https://www.sciopen.com/journal/1998-0124 on Apr. 20, 2026

Just Accepted

TABLE OF CONTENTS (TOC)

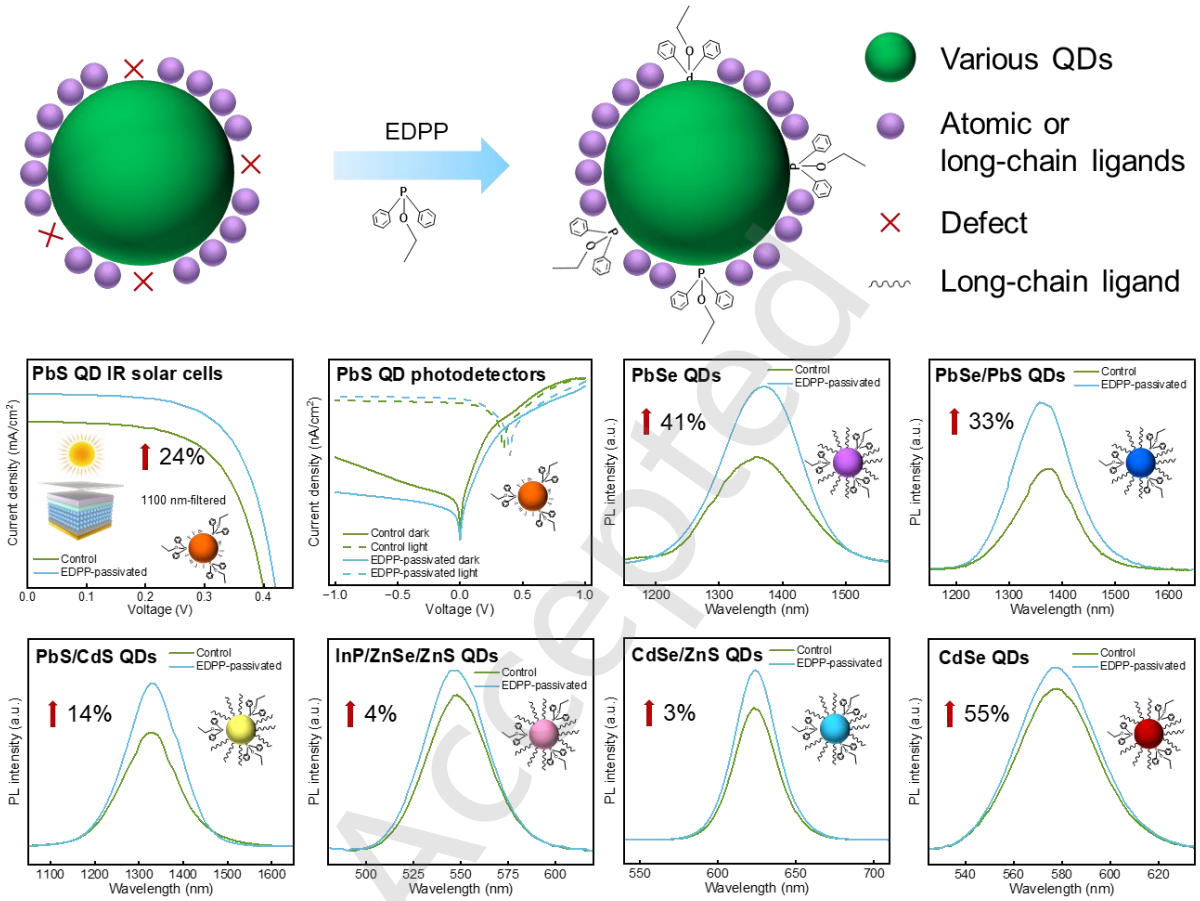

A versatile supplementary passivation strategy is developed by adopting ethoxydiphenylphosphine (EDPP). The EDPP substantially enhances the photoluminescence quantum yields of various QDs and improves the device performance of PbS QD solar cells and photodetectors.

Nano Research

Open Access

Research Article

High-performance quantum dots enabled by supplementary passivation using ethoxydiphenylphosphine

Hao Luo[1], Zhijiao Huang[1], Bo-Yi Deng[1], Chenyu Zhang[1], Yang Liu[1], Ke Peng[2], Rui Long[1], Xiangzhen Deng[1], Daoli Zhang[1], Liang Gao[3], Yanwei Wen[2], Jianbing Zhang[1] ✉, and Jiang Tang[3]

[1] *School of Integrated Circuits, Huazhong University of Science and Technology, Wuhan 430074, China*
[2] *School of Materials Science and Engineering, Huazhong University of Science and Technology, Wuhan 430074, China*
[3] *Wuhan National Laboratory for Optoelectronics, Huazhong University of Science and Technology, Wuhan 430074, China*

Received: 10 February 2026; **Revised:** 4 April 2026; **Accepted:** 20 April 2026

✉ Address correspondence to jbzhang@hust.edu.cn

Cite this article: *Nano Research*, 2026, 19, 94908748 https://doi.org/10.26599/NR.2026.94908748

ABSTRACT: Colloidal quantum dots (QDs) are pivotal to next-generation optoelectronics due to their exceptional quantum confinement effects and solution-processability. However, the high density of surface dangling bonds and vacancy defects inherent in QDs remains a primary bottleneck, inducing non-radiative recombination and limiting device performance. While conventional X-, L-, and Z-type ligand passivation strategies have been developed, achieving a "defect-free" surface for high-performance applications remains challenging. In this work, we introduce ethoxydiphenylphosphine (EDPP) as a universal complementary passivation strategy. For atomic ligand-capped PbS QD systems, EDPP treatment significantly improves QD film quality, enabling solar cells to reach a state-of-the-art infrared power conversion efficiency of 1.50% (under 1100 nm filtering). Furthermore, EDPP-passivated PbS QD photodetectors exhibit a 71.3% reduction in dark current and a peak specific detectivity (D*) of 6.34×10^{12} Jones at 1300 nm. The versatility of EDPP is further validated across various long-chain QD architectures, including InP/ZnSe/ZnS, CdSe/ZnS, PbSe/PbS and so on, where it boosts photoluminescence quantum yield (PLQY) by up to 55.3%. These findings demonstrate that EDPP is a robust tool for precise surface state modulation, paving the way for high-performance, industrial-grade QD optoelectronic applications.

KEYWORDS: quantum dots, supplementary passivation, infrared imaging, solar cells

1 Introduction

Colloidal quantum dots (QDs), as a class of semiconductor nanocrystals characterized by prominent quantum confinement effects, possess unique electronic structures that enable precise bandgap engineering, exceptional optical tunability, and versatile solution-processability [1-4]. These physicochemical merits have effectively bypassed the performance bottlenecks of traditional bulk semiconductors, establishing QDs as pivotal materials in the next generation of optoelectronics [5-7]. Over decades of intensive research, synthetic protocols have matured significantly, allowing for the deterministic control over QD size, composition, and morphology [8-11], which serves as a robust foundation for their practical deployment.

However, the exponential increase in specific surface area as QD size decreases leads to a high density of unsaturated dangling bonds and defects [12-14]. These surface states act as potent charge-carrier recombination centers, which drastically reduce carrier lifetimes, trigger non-radiative recombination, and ultimately degrade the optoelectronic performance of the material [15-18]. Furthermore, such surface defects compromise chemical stability and environmental durability, posing a significant hurdle for the transition of QDs from laboratory-scale prototypes to industrial-grade devices [19, 20]. Consequently, effective surface passivation remains a prerequisite for enhancing QD quality and driving their commercial viability.

Surface passivation strategies are generally categorized into three types based on the nature of the ligand-surface interaction: X-type ligands, which share electrons with unsaturated single-electron sites via covalent bonding; L-type ligands, which donate a lone pair to coordinate with the vacant orbitals of surface metal cations; Z-type ligands, which act as neutral acceptors for the lone pairs of surface anions [21, 22]. While these strategies have mitigated non-radiative recombination and facilitated the integration of QDs into light-emitting diodes [23-26], photodetectors [27-30], and photovoltaics [31-34], conventional single-ligand passivation often fails to achieve a "defect-free" surface. The persistent presence of residual surface states limits the attainment of the high stability and conversion efficiencies required for real-world applications [35]. Therefore, there is an urgent need to develop novel, complementary passivation strategies to achieve more refined control over the QD surface chemistry.

In this study, we designed ethoxydiphenylphosphine (EDPP) as a versatile complementary passivation strategy

for QDs and systematically verified its application. For PbS QDs passivated with atomic ligands (e.g., iodide/bromide), the introduction of EDPP significantly enhances the quality of the resulting thin films. Specifically, Solar cells fabricated using the EDPP-treated film exhibited an infrared (IR) power conversion efficiency (PCE) of 1.50% after filtering with a 1100 nm filter, representing a 24.0% enhancement and ranking among the world's leading levels. When applied to photodetectors, the EDPP-passivated active layer yields a 71.3% reduction in dark current at a -0.1 V bias, while the peak external quantum efficiency (EQE) in the infrared region increases by 37.3%. The specific detectivity (D*) at 1300 nm is more than doubled, reaching 6.34×10^{12} Jones. Meanwhile, the fabricated QD imager exhibited excellent imaging performance. EDPP can also further enhance the passivation of QDs bonded with long-chain ligands, including CdSe/ZnS, CdSe, InP/ZnSe/ZnS, PbS, PbS/CdS, PbSe, and PbSe/PbS QDs. The addition of EDPP leads to a substantial boost in photoluminescence (PL) intensity, with the photoluminescence quantum yield (PLQY) increasing by up to 55.3%. These findings demonstrate that EDPP is a highly adaptable and effective tool for optimizing the performance of diverse QD architectures.

2 Results and discussion

2.1 Mechanism and characterization of EDPP passivation

To evaluate the feasibility of using EDPP as a universal supplementary passivation strategy for QDs, we first analyzed its passivation advantages from both molecular structure and interaction mechanism perspectives. EDPP exhibits excellent structural adaptability, balancing moderate rigidity and flexibility. The phenyl rings provide stability, while the ethoxy chains allow the molecule to conform to QDs with different surface structures. Importantly, the phosphine group in EDPP is an electron-rich functional group with strong coordination affinity toward metal cations on the QD surface [22, 36, 37]. These features make EDPP a highly compatible passivating ligand that effectively satisfies the passivation requirements for surface metal cations.

Figure 1a illustrates the cooperative passivation process of EDPP on PbS QDs. During the liquid-phase ligand exchange, iodide ions displace and remove the long-chain ligands from the QD surface, a process that simultaneously exposes under-coordinated Pb^{2+} defect sites. The subsequent introduction of EDPP into the ink system facilitates supplemental passivation via strong coordination between its electron-rich phosphine groups and these Pb^{2+} sites, leading to a more comprehensive elimination of surface defects. The effectiveness of this cooperative passivation was validated using Fourier transform infrared spectroscopy (FTIR) and X-ray photoelectron spectroscopy (XPS). Compared to the control film (only I^-/Br^--passivated PbS QD film), FTIR spectra (Figure 1b) of the EDPP film (the EDPP-supplemented passivated PbS QD film) reveals four characteristic peaks at 1640, 1439, 1089, and 696 cm^{-1}. These correspond to the C=C stretching vibration of the benzene ring skeleton, one of the characteristic indicator peaks of P-Ph bonds, symmetric stretching of P-O-C, and out-of-plane bending vibrations of monosubstituted benzene rings in EDPP [38], respectively. Meanwhile, the XPS P 2s spectrum of the EDPP film shows a distinct signal peak, whereas no such peak is observed in the control film (Figure 1c). The results of FTIR and XPS P 2s spectra serve as direct evidence for the presence of EDPP in the film. After EDPP treatment, the iodine and bromine contents decrease only slightly while phosphorus appears in the film (Table S1), suggesting that EDPP is introduced mainly as a co-passivating ligand rather than through extensive replacement of the original halide ligands. As shown in Figure 1d, the Pb 4f peaks in the EDPP film shift toward a lower binding energy. In addition, ^{31}P NMR measurements reveal a clear chemical-shift change of the P atom in EDPP after treatment with PbS QDs, and a similar shift is also observed in the EDPP–Pb $(OAc)_2$ system (Figure S1). These results support the coordination between the P atom in EDPP and surface Pb sites on the PbS QDs.

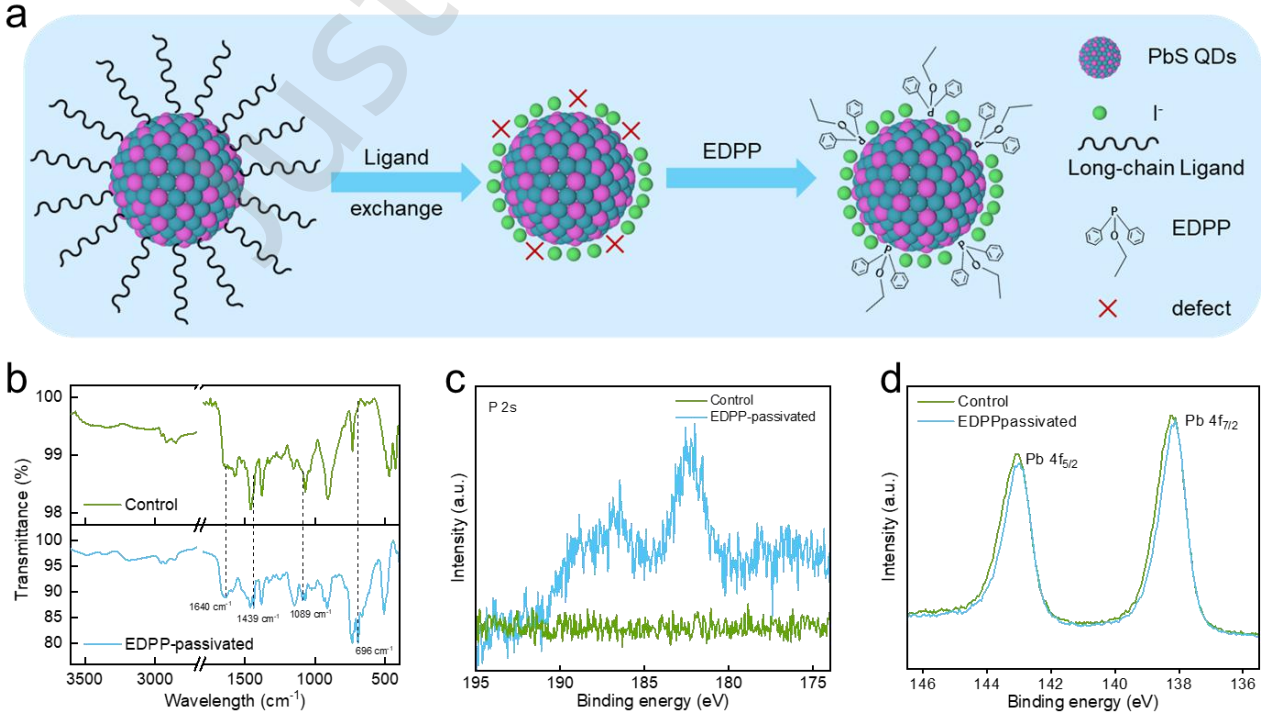

Figure 1. (a) Schematic diagram of ligand exchange and EDPP supplementary passivation process of PbS quantum dots, (b) FT-IR spectra, (c) XPS P 2s spectra and (d) XPS Pb 4f spectra of the control film and the EDPP film.

2.2 Photophysical characteristics of PbS QD films

Optical characterizations were conducted on the PbS QD films with EDPP supplementary passivation. UV-Vis absorption spectra exhibit clear excitonic absorption peaks for both the control film and the EDPP film (Figure 2a). Notably, the peak-to-valley ratio of the EDPP film reaches 6.3, significantly higher than the 2.5 of the control film. In addition, the absorption spectrum of the EDPP film shows an apparent redshift relative to that of the control film. This shift arises because the control film undergoes a blueshift due to butylamine-induced etching of PbS QDs [39-41], whereas EDPP suppresses this etching and better preserves the original size and surface state of the quantum dots. A higher peak-to-valley ratio indicates a narrower size distribution of QDs [42-44]. This improvement is likely due to the more uniform surface passivation provided by EDPP, which suppresses interparticle aggregation and improves the dispersibility and uniformity of QDs in the film.

The PL spectrum of the control film, deviating significantly from a Gaussian distribution, is best fitted with two peaks: a band-edge recombination peak at 1337 nm and a defect-state peak at 1451 nm attributable to surface defects and QDs aggregation (Figure 2b) [45]. In contrast, the PL spectrum of the EDPP film is well-fitted by a single Gaussian peak, indicating that EDPP passivation effectively suppresses defect-related emission and inhibits QD aggregation. Furthermore, the EDPP film shows notably smaller values for the Stokes shift, absorption full width at half maximum (FWHM), and PL FWHM compared to the control film (Figure 2c), supporting the conclusion that EDPP improves the optical quality of the film [46].

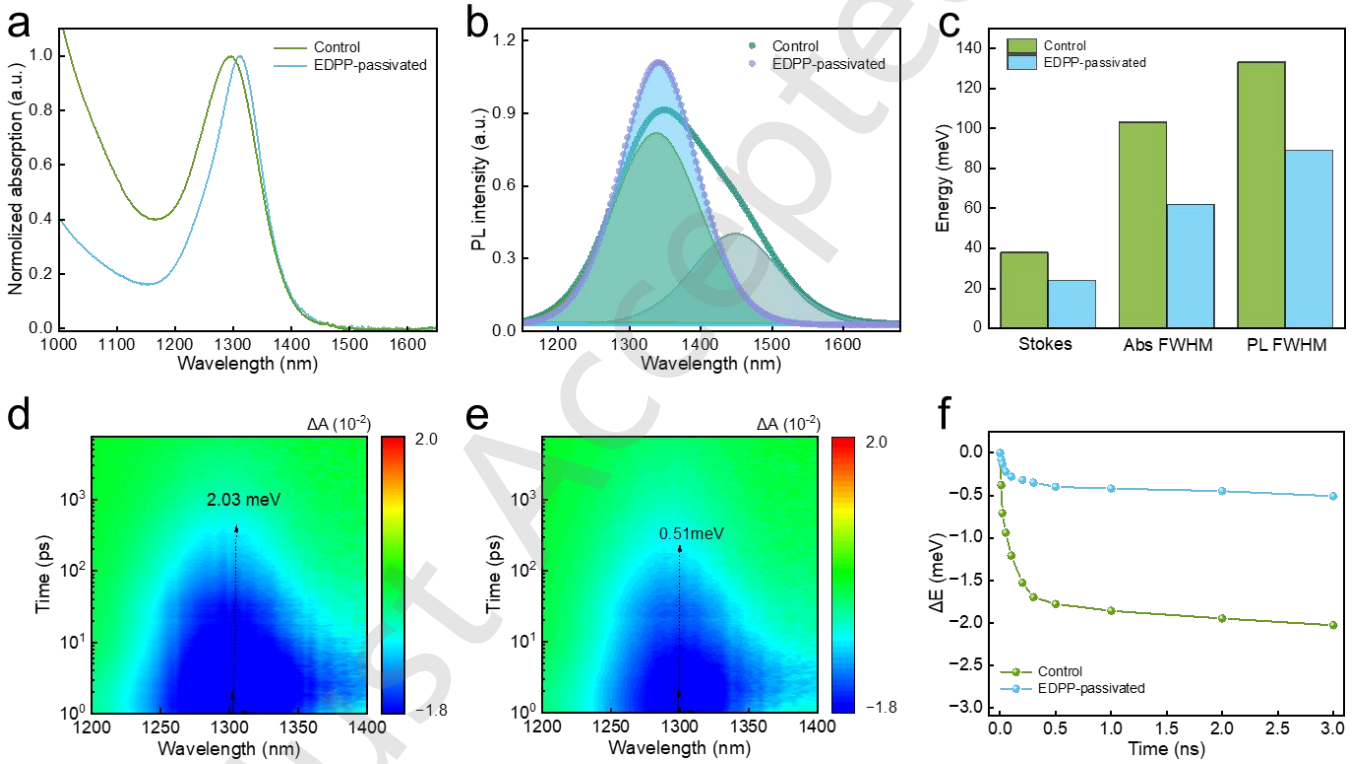

Figure 2. Optical and carrier dynamic characterizations of PbS QD films with/without EDPP supplementary passivation. (a) Absorption spectra and (b) PL spectra of the Control and EDPP QD films, (c) values of Stokes shift, FWHM of exciton absorption peaks, and FWHM of PL peaks, Transient absorption (TA) contour plots of the (d) Control and (e) EDPP films, (f) evolution of the bleach peak energy shift (ΔE) with time (ns) for the Control and EDPP films.

Transient absorption (TA) spectroscopy was used to study carrier dynamics in the films. Contour plots of the broadband TA spectra reveals distinct bleach peaks around the steady-state absorption peaks within a few picoseconds after pump excitation, which gradually weakens over several nanoseconds (Figure 2d and 2e). Compared with the control film, the bleach peak region of the EDPP film is more concentrated with less shifting. Figure 2f quantifies the energy shift of the bleach peak over time. The redshift of the EDPP film is only 0.51 meV, significantly lower than that of the control film (2.03 meV). These results are attributed to the passivation of surface defects by EDPP, which effectively suppresses carrier relaxation toward band-tail states/defect states.

2.3 Device Performance of EDPP-Based PbS QD

Solar cells fabricated using PbS QD films with EDPP supplementary passivation exhibit excellent performance. Figure 3a illustrates the device architecture and corresponding cross-sectional scanning electron microscopy (SEM) image. The device was fabricated on an ITO-patterned glass substrate, with a ZnO layer deposited by magnetron sputtering, followed by spin-coating of PbS-halide (EDPP) and PbS-EDT layers, and thermal evaporation of a gold top electrode. Current density-voltage (*J-V*) measurements revealed that the EDPP device exhibits higher open-circuit voltage (V_{OC}) and short-circuit current density (J_{SC}) compared

to the control device (Figure 3b). Specifically, the EDPP device achieves a V_{OC} of 0.48 V, J_{SC} of 35.6 mA·cm^{-2}, fill factor (FF) of 63.7%, and a PCE of 11.01%, all of which slightly surpass the control values (Table S2).

After filtering with a 1100 nm filter, the infrared (IR) PCE of the EDPP device reaches 1.50%, which is higher than the 1.21% of the control device (Figure 3c). The external quantum efficiency (EQE) spectrum reveals that the EDPP device achieves a response peak of 60.1% in the infrared band (Figure 3d), confirming its outstanding IR photovoltaic performance. The long-term stability of the solar cells was evaluated under ambient air storage conditions, with performance variations shown in Figure S2. After 28 days, the PCE of the control device decreases by 10.3% (from 9.99% to 8.96%, Figure S2a), whereas the EDPP device only shows a 4.2% PCE reduction (from 11.01% to 10.54%, Figure S2b). Figure 3e compares the IR PCE (after 1100 nm filtering) of the EDPP device with those of reported QD solar cells from 2018 to 2025. As illustrated, the IR PCE of the EDPP device is significantly higher than previously reported values, ranking among the world's leading levels. Specific performance details are listed in Table S3.

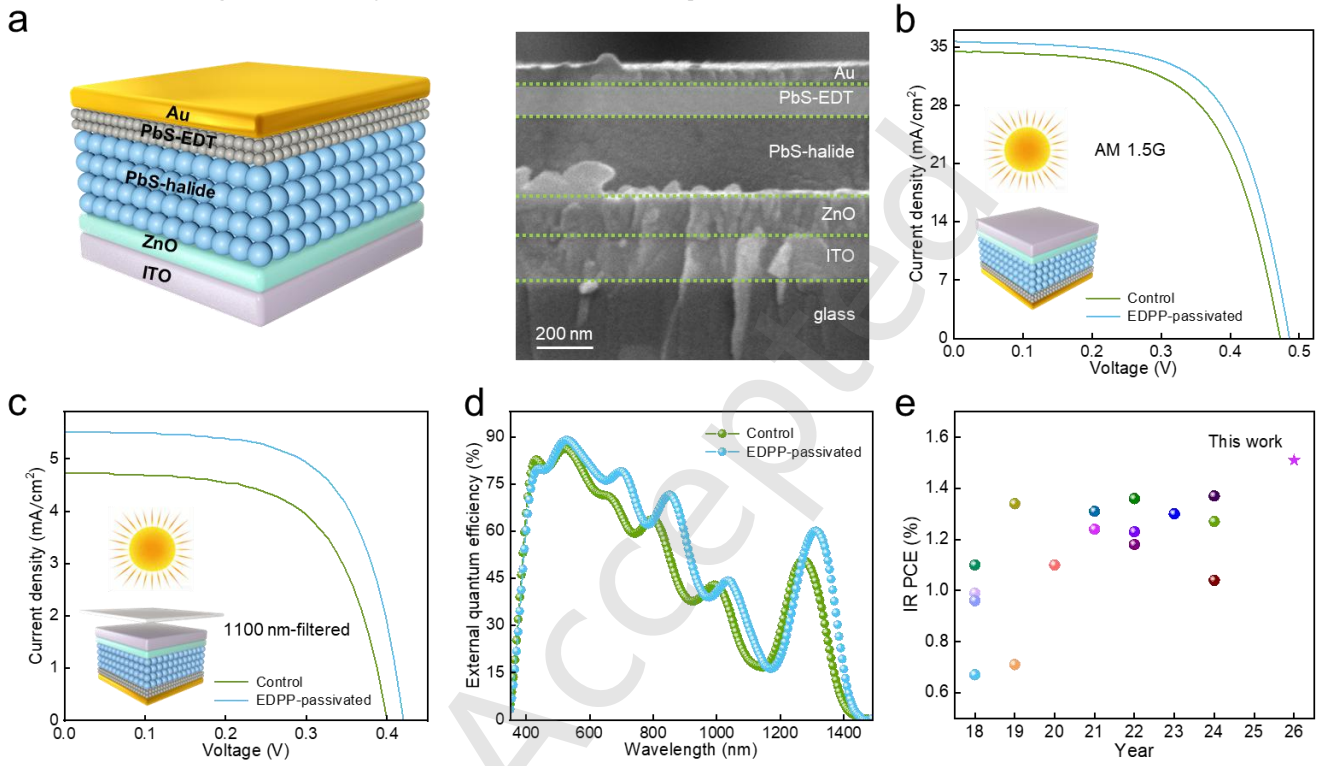

Figure 3. Device structure and performance characterization of EDPP-supplemented passivated PbS QD solar cells. (a) Schematic diagram of the device structure and cross-section SEM image of the solar cell, (b) current *J-V* curves of the Control and EDPP solar cells under AM 1.5G illumination. (c) *J-V* curves of the Control and EDPP solar cells under 1100-nm-filtered illumination, (d) EQE spectra of the Control and EDPP solar cells, (e) comparison of IR-PCE (after 1100-nm filtering) between this work and previous work.

Carrier dynamics were investigated using transient photocurrent (TPC) and transient photovoltage (TPV) measurements (Figure S3). Normalized TPC curves fitted with a single-exponential decay function reveal a shorter carrier extraction time in the EDPP device (3.83 μs) than in the control device (6.31 μs) (Figure S3a), suggesting improved carrier transport and collection efficiency. Normalized TPV decays were fitted with a double-exponential function (Figure S3b), from which the fast (τ_1) and slow (τ_2) recombination lifetimes were extracted. The EDPP device shows extended τ_1 (from 9.12 μs to 14.39 μs) and τ_2 (from 181.14 μs to 266.87 μs), indicating suppressed defect-assisted recombination and longer carrier lifetimes. These results confirm that EDPP passivation effectively reduces trap-mediated recombination.

To further demonstrate the supplementary passivation effect of EDPP, photodetectors were fabricated using the EDPP films, with the device architecture illustrated in Figure 4a. ITO-patterned glass serves as the substrate. A NiO_x layer and the top transparent electrode (ITO) were deposited by magnetron sputtering, PbS-EDT and PbS-halide (EDPP) layers were prepared via spin-coating, a C_{60} layer was formed by thermal evaporation, and a SnO_2 layer was deposited using atomic layer deposition. To optimize the supplementary passivation conditions, devices treated with different EDPP concentrations were compared by their dark and illuminated J-V characteristics (Figure S4). With increasing EDPP concentration, the dark current first decreases and then increases, indicating that an appropriate amount of EDPP can effectively passivate surface defects and suppress defect-assisted leakage current, whereas excessive EDPP may disturb inter-dot charge transport. Among the investigated conditions, the device treated with 1.0% EDPP exhibits the best overall performance and was therefore selected for the following detailed characterization.

Figure 4b shows the *J-V* characteristics measured under ambient conditions at room temperature. The EDPP device exhibits a dark current density of 9.7 nA·cm^{-2} at −0.1 V, substantially lower than that of the control device (33.8 nA·cm^{-2}). Moreover, the dark current increases slower with bias voltage in the EDPP device, indicating superior electrical performance under dark conditions. As shown in Figure 4c,

the EDPP-based photodetector exhibits a broadband photoresponse from 300 nm to 1500 nm, with a peak at 1300 nm aligning with the first exciton absorption of PbS QDs. At peak wavelength, the EQE of the EDPP device is enhanced by 37.3% to reach 68.2%, corresponding to a responsivity of 0.715 A·W^{-1} (Figure S5).

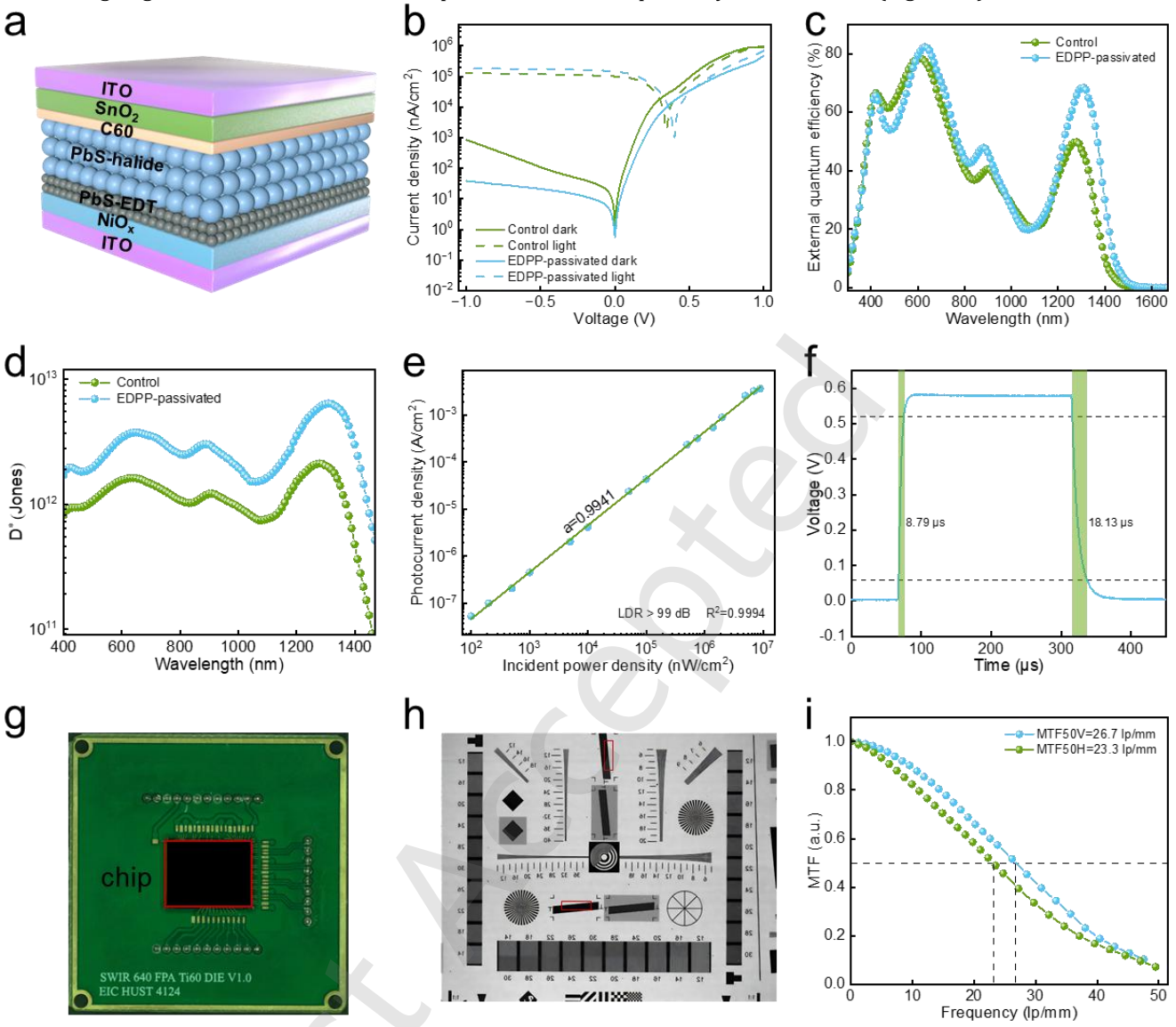

Figure 4. Performance characterization of EDPP-supplemented passivated PbS QD infrared photodetectors and imaging chip. (a) Schematic diagram of the device structure of the infrared photodiode, (b) *J-V* curves, (c) EQE and (d) D* of the Control and EDPP devices, (e) LDR and (f) response time of the EDPP device, (g) Optical photograph of the QD imaging chip bonded on a PCB board, (h) Image of a standard resolution chart captured by the QD imaging chip, (i) MTF curves of the QD imaging chip.

The noise characteristics of the devices are depicted in Figure S6. As frequency increases, the dominant mechanism shifts from 1/f noise to shot noise associated with dark current. The specific detectivity (D*) was calculated using Eq. 1, where A is the active area, I_n is the noise current, R represents the responsivity, and Δf is the bandwidth. The EDPP device achieves a D* value of 6.34×10^{12} Jones at 1300 nm (Figure 4d), significantly higher than the 2.04×10^{12} Jones of the control device. The linear dynamic range (*LDR*), calculated via Eq. 2 using the maximum and minimum detectable optical power (P_{max} and P_{min}), exceeds 99 dB with a responsivity slope of 0.9941, reflecting excellent response linearity. Response speed, a key dynamic parameter, is also improved. The EDPP device shows a rise time (t_r) of 8.79 μs and a fall time (t_f) of 18.13 μs (Figure 4f), faster than those of the control device (15.38 μs and 39.56 μs, respectively; Figure S7). This improvement is attributed to EDPP-mediated surface passivation, which enhances carrier transport and suppresses defect-induced recombination losses.

$$D^* = \frac{R}{I_n} \cdot \sqrt{A \cdot \Delta f} \quad (1)$$

$$LDR = 20 \cdot \log\left(\frac{P_{max}}{P_{min}}\right) \quad (2)$$

Finally, the EDPP-based QD photodetector was integrated with a CMOS readout circuit (640×512 array, 15 μm pixel pitch) to form an imaging chip. Figure 4g shows the QD imaging chip bonded onto a PCB board. An image of a standard resolution chart captured by this chip is displayed in Figure 4h, which clearly reveals the detailed features of the chart. The edge spread function (ESF) was extracted from the red-boxed region using the edge-slope method. The ESF curves rise from 10% to 90% of the maximum luminance, requiring only 0.91 and 1.15 pixels in the horizontal and vertical directions (Figure S8), respectively.

The modulation transfer function (MTF), obtained by differentiating the ESF, yields MTF_{50} values of 26.7 lp/mm horizontally and 23.3 lp/mm vertically (Figure 4i), suggesting outstanding spatial resolution.

2.4 EDPP Passivation on Various QDs

To evaluate the passivation effect of EDPP on QDs capped with long-chain ligands, EDPP was introduced into a solution of PbS QDs peaked at 1300 nm passivated by oleic acid. The results show a remarkable enhancement in the PL intensity of the QD solution, with the PLQY increasing from 17.6% to 23.9% (Figure S9a) and the fluorescence lifetime extending from 420 ns (Figure S9b) to 485 ns (Figure S9c). These results demonstrate that EDPP acts as an effective co-passivating agent for oleic acid-capped PbS QDs in the 1300 nm range. A similar improvement in PL intensity was also observed for PbS QDs with different exciton peaks (900 nm, 1550 nm, and 1650 nm, Figure S10) following EDPP treatment. It should be noted that the PL peak position of PbS QDs is highly sensitive to surface ligand changes and may exhibit redshift, blueshift, or nearly no shift depending on the specific surface chemical environment, without following a universal trend.

Further selection of QDs capped with long-chain ligands was conducted to test the supplementary passivation effect of EDPP, including InP/ZnSe/ZnS, CdSe/ZnS, CdSe, PbS/CdS, PbSe and PbSe/PbS. As shown in Figure 5, the addition of EDPP consistently enhanced the PL intensity and improved the PLQY in all systems. The PLQY and the corresponding enhancement ratios for different quantum dots are summarized in Table S4. Notably, the maximum increase in PLQY reaches 55.3%. This universal enhancement is attributed to the strong coordination between the phosphine group in EDPP and the metal cations on the QD surface [47, 48], which helps passivate unsaturated sites and suppress non-radiative recombination pathways. Together, these findings confirm the broad applicability of EDPP as a supplementary passivating ligand for QDs spanning various compositions, core/shell structures, and sizes.

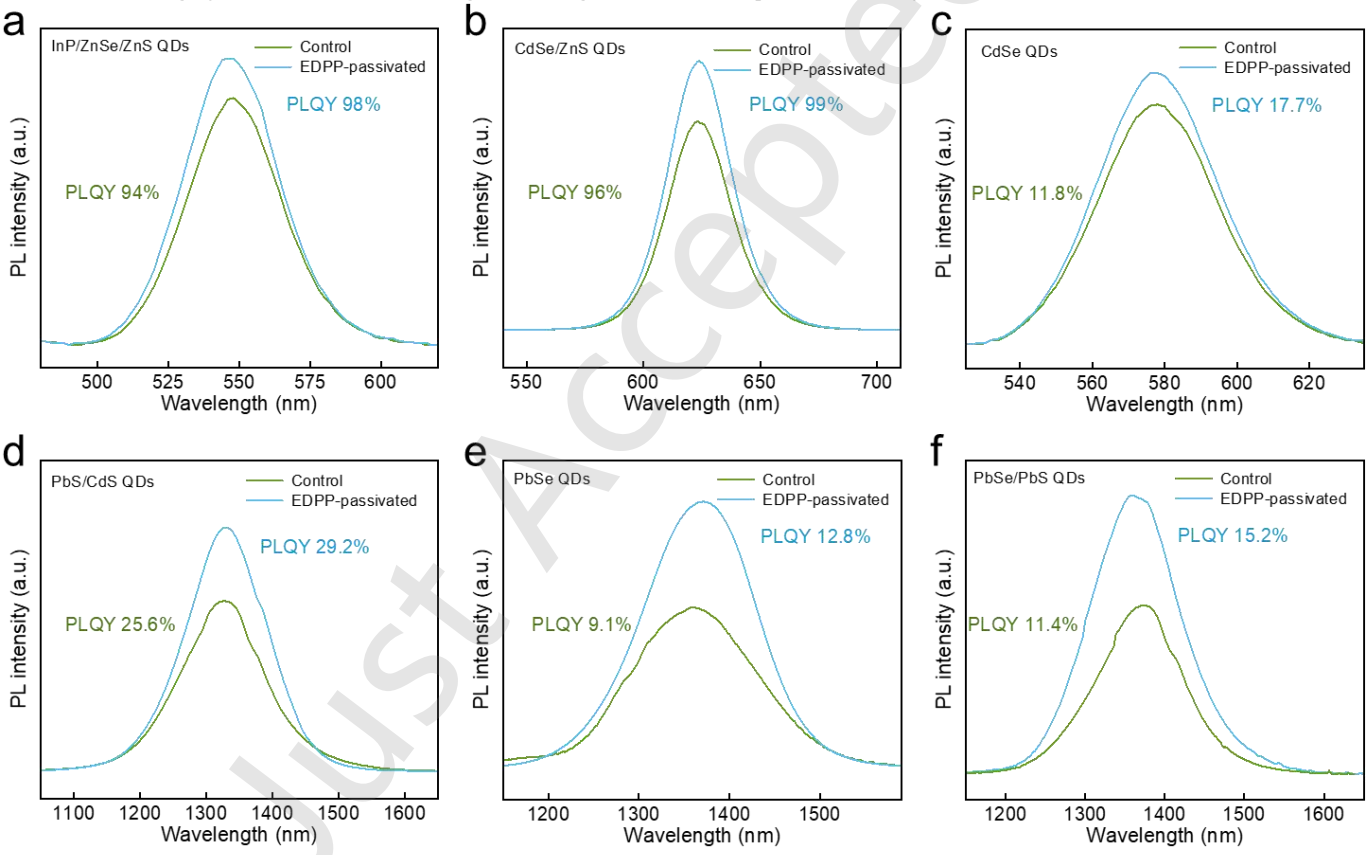

Figure 5. PL spectra of diverse QD systems with/without EDPP supplementary passivation. (a) InP/ZnSe/ZnS, (b) CdSe/ZnS, (c) CdSe, (d) PbS/CdS, (e) PbSe, (f) PbSe/PbS.

3 Conclusions

In summary, we have demonstrated EDPP as a versatile and effective supplementary passivation strategy for QDs. Mechanistic investigations involving FTIR and XPS revealed that the electron-rich phosphine group of EDPP strongly coordinates with surface cations, effectively neutralizing trap states. In atomic ligand-capped PbS QD systems, EDPP-based passivation yields solar cells with an infrared PCE of 1.50% under 1100 nm filtering. Photodetectors incorporating EDPP-treated QDs exhibit a 71.3% reduction in dark current and a specific detectivity of 6.34×10^{12} Jones, while the resulting imaging chip demonstrates high-resolution capability. Beyond PbS QDs, EDPP shows notable universality across various QD systems such as InP, CdSe, PbSe and their core/shell structures, achieving PLQY enhancements of up to 55.3%. This work establishes a complementary passivation strategy for improving QD quality and provides a viable pathway for developing high-performance optoelectronic devices.

4 Experimental

4.1 Synthesis of QDs

Lead chloride (PbCl2, 99.99%), Lead bromide (PbBr2,

99.99%)Lead iodide (PbI2, 99.99%), Lead(II) oxide (PbO, 99.9%), Zinc stearate (10-12%), Bis (trimethylsilyl) sulfide (TMS, 97.0%), Thioacetamide (TAA, 99%), Octadecene (ODE, 90.0%), Oleylamine (OLA, 80-90%), Octylamine (98%), Octane (≥99.5%), Oleic acid (OA, 90%), Acetonitrile (ACN, ≥99.5%), N, N-Dimethylformamide (DMF, 99.5%), ethanol (EtOH, ≥99.7%), 1,2-ethanedithiol (EDT, 97%), Butylamine (BTA, 99.5%), Ethyl acetate (≥99.5%), n-Hexane (≥97.0%), Butylamine (BTA, 99%), Cadmium acetate (Cd(Ac)2, 99%) and Selenourea (≥98%) were purchased from Sinopharm Chemical Reagent.

4.2 Synthesis of QDs

InP/ZnSe/ZnS QDs were synthesized according to the previously reported method [49]. The CdSe/ZnS QDs were obtained from Wuhan Jiayuan Quantum Dots Technology Development Co., Ltd. PbSe/PbS QDs were synthesized according to the previously reported method [50]. PbSe QDs were synthesized according to the previously reported method [11]. PbS QDs exhibiting an absorption peak at 880 nm were synthesized by thermal injection following a reported procedure [48]. PbS QDs with absorption peaks at 900, 1300, 1400, 1550, and 1650 nm were synthesized via a reported cation-exchange method [10].

CdSe QDs is synthesized according to the following process. A mixture of cadmium oxide (3.072 g), 1-octadecene (50.0 mL), and oleic acid (25.0 mL) was added to a 250 mL three-neck flask. The flask was evacuated under vacuum at room temperature, heated to 100 °C, and held at that temperature for 10 minutes. Under a nitrogen atmosphere, the mixture was then heated to 250 °C until it became colorless, cooled to 180 °C, and subsequently cooled to room temperature in a water bath while maintaining vacuum. Under nitrogen at room temperature, 6.0 mL of 1.0 mol/L DPP-Se was injected into the flask. The reaction proceeded at 120 °C for 25 minutes, after which 5.0 mL of 1 mol/L TOP-Se was added dropwise at a rate of 1 mL/min. The reaction was immediately quenched by cooling upon completion of the addition.

PbS/CdS QDs is synthesized according to the following process. PbS QDs with an absorption peak at 1400 nm were dispersed in 1-octadecene to obtain a 50.0 mg/mL stock solution for subsequent use. In a typical cation exchange procedure, cadmium oxide (2.0 g), oleic acid (12.0 mL), and 1-octadecene (25.0 mL) were combined in a three-neck flask and evacuated under vacuum at 140 °C for 30 minutes. The mixture was then heated to 250 °C until a colorless solution formed, cooled to 80 °C, and injected with the as-prepared PbS QD solution. The reaction was monitored in real time by absorption spectroscopy and quenched by cooling in a water bath once the first exciton peak shifted to 1300 nm. The crude product was centrifuged at 8000 rpm for 3 minutes to remove insoluble residues. After adding an equal volume of ethanol, the mixture was centrifuged again for 5 minutes to isolate the solid PbS/CdS QDs.

4.3 Solution-phase ligand exchange

A ligand solution was prepared by completely dissolving 2.67 mmol of PbI_2 and 0.58 mmol of $PbBr_2$ in 10 mL of ultra-dry DMF, followed by filtration. Separately, 10 mg of 1300 nm PbS QDs were dispersed in 10.0 mL of octane. Slowly pour the QD solution into the ligand solution and shake for one minute to transfer the PbS quantum dots from the non-polar octane phase to the polar DMF phase, and replace the long-chain oleic acid ligand with the halogen ligand. The resulting ligand-exchanged QDs were washed twice with octane to remove residual oleic acid, then collected by centrifugation and vacuum-dried for 1 h. For film fabrication: The control film was prepared by dissolving the ligand-exchanged PbS QDs at 350 mg/mL in a mixed solvent of DMF and BTA (volume ratio 1:4). The EDPP film was obtained by dissolving the QDs at the same concentration in a ternary solvent mixture of DMF, BTA, and EDPP (volume ratio 1:4:0.01).

4.4 Solar cell fabrication

The etched ITO substrates were sequentially cleaned by ultrasonication in deionized water, isopropyl alcohol, and ethanol, each for 30 minutes. A zinc oxide (ZnO) layer was deposited onto the cleaned ITO substrates via magnetron sputtering at room temperature. This process was conducted under an argon/oxygen flow ratio of 99:1, with a chamber pressure of 2 Pa, a sputtering power of 150 W, and a duration of 40 minutes. The active layer was fabricated by spin-coating liquid-phase ligand-exchanged PbS QDs at 2500 rpm, followed by annealing at 90 °C for 10 minutes within a glovebox. Subsequently, a PbS-EDT film was prepared from 880 nm PbS QDs via solid-phase ligand exchange, following the basic procedure reported in our previous work [51]. The film thickness was re-optimized for the present device design, and a total of four solid-phase ligand-exchange cycles were carried out. Finally, a patterned top Au electrode was deposited via thermal evaporation, with a chamber pressure of less than 8.0×10^4 Pa and a deposition rate of 0.5 $Å \cdot s^{-1}$. The effective area of the electrode was 0.0706 cm^2.

4.5 Photodetector fabrication

The etched ITO is cleaned in a manner consistent with the substrate of the solar cell. A nickel oxide (NiO_x) layer was deposited onto the cleaned ITO substrates via magnetron sputtering at room temperature. The process was carried out under an argon atmosphere at a chamber pressure of 5 Pa, with a sputtering power of 100 W applied for 15 minutes. A PbS-EDT film was prepared through solid-phase ligand exchange using 880 nm PbS QDs, following a previously reported procedure[51]. The active layer was fabricated by spin-coating liquid-phase ligand-exchanged PbS QDs at 2500 rpm, followed by annealing at 90 °C for 10 minutes within a glovebox. Subsequently, a 7 nm-thick C_{60} layer was thermally evaporated at a deposition rate of 0.08 $Å \cdot s^{-1}$. This was followed by the deposition of a 40 nm-thick SnO_2 layer via atomic layer deposition (ALD). Finally, a transparent ITO top electrode was deposited by magnetron sputtering at room temperature under an argon pressure of 2 Pa, using a sputtering power of 100 W for 15 minutes. The active area of the resulting device was 0.0706 cm^2.

4.6 Imager fabrication

The readout integrated circuits (ROICs) were obtained from Wuhan InRight Infrared Technology Co., Ltd. All functional layers of the device were deposited directly onto the ROICs using a process analogous to that employed for standalone photodetectors. After SnO deposition, laser etching was performed to expose the common electrode contacts of the ROIC for electrical connection to the subsequently deposited ITO top electrode. A second laser etching step was carried

out following ITO sputtering to define the bonding pads. Finally, wire bonding was conducted, and the imaging chip was assembled with a packaging mold to enable imaging functionality.

4.7 Measurement and characterization

The surface morphology of the film was characterized by scanning electron microscopy (SEM, GeminiSEM 300). The absorption spectra of PbS QD films on quartz substrates were recorded using a UV-Vis-NIR spectrophotometer (Shimadzu UV 3600 Plus). Film composition was analyzed by X-ray photoelectron spectroscopy (XPS, AXIS SUPRA+). PL spectra and lifetimes were acquired on a fluorescence spectrometer (QuantaMaster 8000), while transient absorption measurements were performed using a femtosecond transient absorption spectrometer (Ultrafast Systems Helios). The J-V characteristics of the devices were measured in the dark and under 1300 nm LED (M1300L3) illumination using a semiconductor parameter analyzer (Agilent B1500A). The EQE was determined from spectral response measurements (LightSky Tech LST-QE system). The LDR was evaluated under varying light intensities using the same Agilent B1500A analyzer. For TPC, TPV, response time and -3 dB bandwidth measurements, a 635 nm laser was used as the excitation source, with the signal recorded by an oscilloscope (Keysight DSO-S 054A). Noise current for specific detectivity calculation was measured in a dark shielded chamber using a preamplifier (SR570) and lock-in amplifier (SR850). The J-V characteristics of solar cells were evaluated under simulated sunlight (Model 9119).

Data availability

All data needed to support the conclusions in the paper are presented in the manuscript and/or the Electronic Supplementary Material. Additional data related to this paper may be requested from the corresponding author upon request.

Acknowledgements

This work was supported by the National Key Research and Development Program of China (2021YFA0715502), the National Natural Science Foundation of China (62475084, U24A20510, 62374068), Major Program (JD) of Hubei Province (2023BAA017), Hubei Province Technological Innovation Program Project (2024BCB094), the Innovation Project of Optics Valley Laboratory (No. OVL2023ZD002), International Science and Technology Cooperation Project of Hubei Province (2024EHA027), Wuhan Science and Technology Project (No. 2025040601030118), Interdisciplinary Research Program of HUST (2025JCYJ008), the China Postdoctoral Science Foundation (No. 2022M721243), and Shenzhen Science and Technology Program (JCYJ20241202123506009). The authors thank the ROIC and imaging system support of Wuhan InRight Technology Co., Limited, and the Testing Center of Huazhong University of Science and Technology.

Declaration of competing interest

All the contributing authors report no conflict of interests in this work.

Author contribution statement

H.L.: Data curation, project administration, validation, writing manuscript, and experimental design. Z.J.H.: Data curation, validation, project administration, experimental design. B.Y.D.: Data curation, validation, project administration, experimental design. C.Y.Z.: Data curation, validation, experimental design. Y.L.: Data curation, experimental design. K. P.: Data curation, experimental design. R.L.: Data curation, experimental design. X.Z.D.: Data curation, experimental design. D.L.Z.: Supervision, Project administration. L.G.: Supervision, Project administration. Y.W.W.: Supervision, Project administration. J.B.Z.: Validation, Supervision, Project administration, writing manuscript, Funding acquisition. J.T.: Supervision, Project administration. All the authors have approved the final manuscript."

Informed consent

Not applicable.

Ethics statement

Not applicable.

Use of AI statement

None.

References

[1] Sukhovatkin, V.; Hinds, S.; Brzozowski, L. and Sargent, E. H. Colloidal quantum-dot photodetectors exploiting multiexciton generation. Science 2009, 324, 1542-1544.

[2] Xu, K. M.; Xiao, X. B.; Zhou, W. J.; Jiang, X. Y.; Wei, Q.; Chen, H.; Deng, Z.; Huang, J.; Chen, B. L. and Ning, Z. J. Inverted Si: PbS colloidal quantum dot heterojunction-based infrared photodetector. ACS Appl. Mater. Interfaces 2020, 12(13), 15414-15421.

[3] Xue, X. M.; Hao, Q. and Chen, M. L. Very long wave infrared quantum dot photodetector up to 18 μm. Light:Sci. Appl. 2024, 13(1), 89.

[4] Brus, L. E. Electron-electron and electron-hole interactions in small semiconductor crystallites: the size dependence of the lowest excited electronic state. J. Chem. Phys. 1984, 80(9), 4403-4409.

[5] Wu, X. G.; Ji, H. L.; Yan, X. L. and Zhong, H. Z. Industry outlook of perovskite quantum dots for display applications. Nat. Nanotechnol. 2022, 17, 813-816.

[6] Liu, M. X.; Yazdani, N.; Yarema, M.; Jansen, M.; Wood, V. and Sargent, E. H. Colloidal quantum dot electronics. Nat. Electron. 2021, 4(8), 548-558.

[7] Zhong, H. Z. and Wang, Y. T. Quantum dots on demand. Nat. Photonics 2020, 14(2), 65-66.

[8] Zhang, Y. Z.; Zhang, C.; Li, B.; Liu, R. X.; Zhang, Y. D.; Shao, Z. C.; Liu, L. M.; Liu, G. Q.; Wu, L.; Zheng, X. S.; Li, Y. and Yu, S. H. Laser - induced size - focusing synthesis of high - quality colloidal quantum dots. Angew. Chem., Int. Ed. 2025, e17547.

[9] Li, B. H.; Duan, Z. H.; Zeng, W. X.; Bu, Y. C.; Yuan, Z.; Jiang, Y. D. and Tai, H. L. Advances in PbX (X = S, Se, Te) quantum - dot photodetectors. Laser Photonics Rev. 2025, e01759.

[10] Xia, Y.; Liu, S. S.; Wang, K.; Yang, X. K.; Lian, L. Y.; Zhang, Z. M.; He, J. G.; Liang, G. J.; Wang, S.; Tan, M. L.; Song, H. S.; Zhang, D. L.; Gao, J. B.; Tang, J.; Beard, M. C. and Zhang, J. B. Cation - exchange synthesis of highly monodisperse PbS quantum dots from ZnS nanorods for efficient infrared solar cells. Adv. Funct. Mater. 2019, 30(4), 1907379.

[11] Lian, L. Y.; Xia, Y.; Zhang, C. W.; Xu, B.; Yang, L.; Liu, H.; Zhang, D. L.; Wang, K.; Gao, J. B. and Zhang, J. B. In situ tuning the reactivity of selenium precursor to synthesize wide range size, ultralarge-scale, and ultrastable PbSe quantum dots. Chem. Mater. 2018, 30(3), 982-989.

[12] Boles, M. A.; Ling, D.; Hyeon, T. and Talapin, D. V. The surface science of nanocrystals. Nat. Mater. 2016, 15(3), 364-364.

[13] Lee, G.; Lee, S. Y.; Park, S.; Jang, S. H.; Park, H. K.; Choi, I.; Park, J. and Choi, J. Highly effective surface defect passivation of perovskite quantum dots for excellent optoelectronic properties. J. Mater. Res. Technol. 2022, 18, 4145-4155.

[14] Xue, J. J.; Wang, R. and Yang, Y. The surface of halide perovskites from nano to bulk. Nat. Rev. Mater. 2020, 5(11), 809-827.

[15] Mann, J. G.; Kostyurina, E.; Döblinger, M.; Nickel, B.; Feldmann, J. and Ghimire, S. Diminishing surface defects in silver indium sulfide quantum dots enables bandgap‐excitonic characteristics. Adv. Opt. Mater. 2025, 13(34), e00434.

[16] Yang, M. J.; Kim, S. J.; Kim, T. H.; Ahn, H.; Lee, M. J.; Kim, Y. and Shim, J. W. Bi-synergistic ligand-mediated passivation of surface defects for highly efficient and stable cesium-lead-iodide perovskite quantum dot photovoltaics. Mater. Horiz. 2026, 13, 1906-1917.

[17] Zhu, H. W.; Tong, G. Q.; Li, J. C.; Tao, X. Y.; Shen, Y.; Sheng, Y. Y.; Shi, L.; Xie, F. M.; Tang, J. X. and Jiang, Y. Acid‐etching induced metal cation competitive lattice occupancy of perovskite quantum dots for efficient pure‐blue QLEDs. Interdiscip. Mater. 2024, 3(3), 437-447.

[18] Kumar, S.; Cocchi, C. and Steenbock, T. Surface defects and symmetry breaking impact on the photoluminescence of InP quantum dots. Nano Lett. 2025, 25(26), 10588-10593.

[19] Jiang, R. Q.; Wu, H. W.; Manzani, D.; Zhang, W. C. and Liu, C. Effect of surface defects on photoluminescence properties of CdSe quantum dots in glasses. Appl. Surf. Sci. 2023, 622, 156931.

[20] Wang, C. and Myoung, J. M. Spatially confined synthesis of $CsPbBr_3$ quantum dots for high-performance pure-blue light-emitting diodes. Matter 2025, 9, 102416.

[21] Owen, J. The coordination chemistry of nanocrystal surfaces. Science 2015, 347, 615-616.

[22] Kirkwood, N.; Monchen, J. O. V.; Crisp, R. W.; Grimaldi, G.; Bergstein, H. A. C.; du Fossé, I.; van der Stam, W.; Infante, I. and Houtepen, A. J. Finding and fixing traps in II-VI and III-V colloidal quantum dots: the importance of Z-type ligand passivation. J. Am. Chem. Soc. 2018, 140(46), 15712-15723.

[23] Moon, H.; Lee, C. M.; Lee, W.; Kim, J. and Chae, H. Stability of quantum dots, quantum dot films, and quantum dot light‐emitting diodes for display applications. Adv. Mater. 2019, 31(34), 1804294.

[24] Bian, Y. Y.; Yan, X. H.; Chen, F.; Li, Q.; Li, B.; Hou, W. J.; Lu, Z.; Wang, S. B.; Zhang, H.; Zhang, W. J.; Zhang, D. D.; Tang, A. W.; Fan, F. J. and Shen, H. B. Efficient green InP-based QD-LED by controlling electron injection and leakage. Nature 2024, 635(8040), 854-859.

[25] Jin, W. X.; He, S. Y.; Lu, X. Y.; Zhu, X. T.; Liu, D. J.; Sun, G. L.; Hao, Y. L.; Chen, Z. Y.; Wang, C. Y.; Zeng, J. J.; Zheng, Z.; Yan, X. L.; Yan, Y. R.; Wu, L. J.; Lin, X. F.; Hou, W. J.; Cao, W. R.; Liu, C.; Liang, X. C.; Gao, Y.; Deng, Y. Z.; Cao, K. S.; Yang, Y. G.; Gao, F. and Jin, Y. Z. Water-induced high-performance quantum-dot light-emitting diodes. Nat. Photonics 2025, 19(11), 1233-1239.

[26] Liu, M. M.; Wan, Q.; Wang, H. M.; Carulli, F.; Sun, X. C.; Zheng, W. L.; Kong, L.; Zhang, Q.; Zhang, C. Y.; Zhang, Q. G.; Brovelli, S. and Li, L. Suppression of temperature quenching in perovskite nanocrystals for efficient and thermally stable light-emitting diodes. Nat. Photonics 2021, 15(5), 379-385.

[27] Kim, B.; Lee, S. Y.; Ko, H.; Lee, J.; Song, H.; Cho, S.; Kim, Y. H.; Lee, M.-H. and Lee, J.-Y. Ultrahigh-gain colloidal quantum dot infrared avalanche photodetectors. Nat. Nanotechnol. 2024, 20(2), 237-245.

[28] Leemans, J.; Pejović, V.; Georgitzikis, E.; Minjauw, M.; Siddik, A. B.; Deng, Y. H.; Kuang, Y. H.; Roelkens, G.; Detavernier, C.; Lieberman, I.; Malinowski, P. E.; Cheyns, D. and Hens, Z. Colloidal III-V quantum dot photodiodes for short‐wave infrared photodetection. Adv. Sci. 2022, 9(17), 2200844.

[29] Yu, M. X.; Yang, J.; Zhang, X. C.; Yuan, M. H.; Zhang, J. B.; Gao, L.; Tang, J. and Lan, X. Z. In‐synthesis Se‐stabilization enables defect and doping engineering of HgTe colloidal quantum dots. Adv. Mater. 2024, 36(27), 2311830.

[30] Chen, M. L.; Hao, Q.; Luo, Y. N. and Tang, X. Mid-infrared intraband photodetector via high carrier mobility HgSe colloidal quantum dots. ACS Nano 2022, 16(7), 11027-11035.

[31] Yuan, M. J.; Liu, M. X. and Sargent, E. H. Colloidal quantum dot solids for solution-processed solar cells. Nat. Energy 2016, 1(3), 16016.

[32] Cao, Y. M.; Stavrinadis, A.; Lasanta, T.; So, D. and Konstantatos, G. The role of surface passivation for efficient and photostable PbS quantum dot solar cells. Nat. Energy 2016, 1(4), 16035.

[33] Wang, W.; Feng, W. L.; Du, J.; Xue, W. N.; Zhang, L. L.; Zhao, L. L.; Li, Y. and Zhong, X. H. Cosensitized quantum dot solar cells with conversion efficiency over 12%. Adv. Mater. 2018, 30(11), 1705746.

[34] Shi, G. Z.; Ding, X. B.; Liu, Z. K.; Liu, Y.; Chen, Y. F.; Liu, C.; Ni, Z. T.; Wang, H. B.; Ito, K.; Igarashi, K.; Feng, K.; Zhang, K. C.; Lüer, L.; Chen, W.; Lyu, X. Y.; Song, B.; Sun, X.; Yuan, L.; Liu, D.; Li, Y. S.; Lu, K. Y.; Deng, W.; Li, Y. Y.; Müller Buschbaum, P.; Li, T.; Zhong, J.; Uchida, S.; Kubo, T.; Li, N.; Luther, J. M.; Segawa, H.; Shen, Q.; Brabec, C. J. and Ma, W. L. Overcoming efficiency and cost barriers for large-area quantum dot photovoltaics through stable ink engineering. Nat. Energy 2025, 10(5), 592-604.

[35] Liu, P. L.; Lu, S. C.; Liu, J.; Xia, B.; Yang, G. Y.; Ke, M.; Zhao, X. Z.; Yang, J. R.; Liu, Y. X.; Ge, C. Y.; Liang, G. J.; Chen, W.; Lan, X. Z.; Zhang, J. B.; Gao, L. and Tang, J. Double‐ended passivator enables dark‐current‐suppressed colloidal quantum dot photodiodes for CMOS‐integrated infrared imagers. InfoMat 2023, 6(1), e12497.

[36] Kim, J.; Ouellette, O.; Voznyy, O.; Wei, M.; Choi, J.; Choi, M. J.; Jo, J. W.; Baek, S. W.; Fan, J.; Saidaminov, M. I.; Sun, B.; Li, P.; Nam, D. H.; Hoogland, S.; Lu, Z. H.; García de Arquer, F. P. and Sargent, E. H. Butylamine‐catalyzed synthesis of nanocrystal inks enables efficient infrared CQD solar cells. Adv. Mater. 2018, 30(45), 1803830.

[37] Beygi, H.; Sajjadi, S. A.; Babakhani, A.; Young, J. F. and van Veggel, F. C. J. M. Surface chemistry of as-synthesized and air-oxidized PbS quantum dots. Appl. Surf. Sci. 2018, 457, 1-10.

[38] Jo, S. H.; Kang, D. H.; Shim, J.; Jeon, J.; Jeon, M. H.; Yoo, G.; Kim, J.; Lee, J.; Yeom, G. Y.; Lee, S.; Yu, H. Y.; Choi, C. and Park, J. H. A high-performance WSe_2/h-BN photodetector using a triphenylphosphine (PPh_3)-based n-doping technique. Adv. Mater. 2016, 28(24), 4824-4831.

[39] Sliz, R.; Lejay, M.; Fan, J. Z.; Choi, M.-J.; Kinge, S.; Hoogland, S.; Fabritius, T.; García de Arquer, F. P. and Sargent, E. H. Stable colloidal quantum dot inks enable inkjet-printed high-sensitivity infrared photodetectors. ACS Nano 2019, 13(10), 11988-11995.

[40] Beygi, H.; Sajjadi, S. A.; Babakhani, A.; Young, J. F. and van Veggel, F. C. J. M. Solution phase surface functionalization of PbS nanoparticles with organic ligands for single-step deposition of p-type layer of quantum dot solar cells. Appl. Surf. Sci. 2018, 459, 562-571.

[41] Xu, J. X.; Voznyy, O.; Liu, M. X.; Kirmani, A. R.; Walters, G.; Munir, R.; Abdelsamie, M.; Proppe, A. H.; Sarkar, A.; García de Arquer, F. P.; Wei, M.; Sun, B.; Liu, M.; Ouellette, O.; Quintero-Bermudez, R.; Li, J.; Fan, J.; Quan, L.; Todorovic, P.; Tan, H.; Hoogland, S.; Kelley, S. O.; Stefik, M.; Amassian, A. and Sargent, E. H. 2D matrix engineering for homogeneous quantum dot coupling in photovoltaic solids. Nat. Nanotechnol. 2018, 13(6), 456-462.

[42] Voznyy, O.; Levina, L.; Fan, J. Z.; Askerka, M.; Jain, A.; Choi, M. J.; Ouellette, O.; Todorović, P.; Sagar, L. K. and Sargent, E. H. Machine learning accelerates discovery of optimal colloidal

quantum dot synthesis. ACS Nano 2019, 13(10), 11122-11128.

[43] He, J. G.; Luo, M.; Hu, L.; Zhou, Y. L.; Jiang, S. L.; Song, H. S.; Ye, R.; Chen, J.; Gao, L. and Tang, J. Flexible lead sulfide colloidal quantum dot photodetector using pencil graphite electrodes on paper substrates. J. Alloys Compd. 2014, 596, 73-78.

[44] Kim, T.; Park, S. and Jeong, S. Diffusion dynamics controlled colloidal synthesis of highly monodisperse InAs nanocrystals. Nat. Commun. 2021, 12(1), 3013.

[45] Gilmore, R. H.; Liu, Y.; Shcherbakov Wu, W.; Dahod, N. S.; Lee, E. M. Y.; Weidman, M. C.; Li, H.; Jean, J.; Bulović, V.; Willard, A. P.; Grossman, J. C. and Tisdale, W. A. Epitaxial dimers and auger-assisted detrapping in PbS quantum dot solids. Matter 2019, 1(1), 250-265.

[46] Voznyy, O.; Levina, L.; Fan, F.; Walters, G.; Fan, J. Z.; Kiani, A.; Ip, A. H.; Thon, S. M.; Proppe, A. H.; Liu, M. and Sargent, E. H. Origins of stokes shift in PbS nanocrystals. Nano Lett. 2017, 17(12), 7191-7195.

[47] Chen, J. W.; Liu, X. Y.; Cai, B.; Cheng, Y. Z.; Wen, H.; Zhu, D. L.; Xiong, Y. N.; Dai, L. J.; Yan, X. H.; Xiang, B. X.; Luo, X. Y.; Feng, W. J.; Du, J. Y.; Dong, S. Y.; Shan, Q. S.; Chen, S. L.; Zeng, H. B.; Xiong, Q. H.; Duan, L. and Ma, D. X. Lattice-matched molecular-anchor design for high-performance perovskite quantum dot light-emitting diodes. Nat. Commun. 2025, 16(1), 8201.

[48] Liu, Z.; Deng, C.; Su, L. W.; Wang, D.; Jiang, Y. S.; Tsuboi, T. J. and Zhang, Q. S. Efficient intramolecular charge-transfer fluorophores based on substituted triphenylphosphine donors. Angew. Chem., Int. Ed. 2021, 60(27), 15049-15053.

[49] Cheng, Y. B.; Li, Q.; Chen, M. Y.; Chen, F.; Wu, Z. H. and Shen, H. B. High-brightness green InP-based QLEDs enabled by in-situ passivating core surface with zinc myristate. Mater. Futures 2024, 3(2), 025201.

[49] Liu, S. S.; Zhang, C. J.; Li, S. Y.; Xia, Y.; Wang, K.; Xiong, K.; Tang, H. D.; Lian, L. Y.; Liu, X. X.; Li, M. Y.; Tan, M. L.; Gao, L.; Niu, G. D.; Liu, H.; Song, H. S.; Zhang, D. L.; Gao, J. B.; Lan, X. Z.; Wang, K.; Sun, X. W.; Yang, Y.; Tang, J. and Zhang, J. B. Efficient infrared solar cells employing quantum dot solids with strong inter‐dot coupling and efficient passivation. Adv. Funct. Mater. 2020, 31(9), 2006864.

[50] Miller, E. M.; Kroupa, D. M.; Zhang, J. B.; Schulz, P.; Marshall, A. R.; Kahn, A.; Lany, S.; Luther, J. M.; Beard, M. C.; Perkins, C. L. and van de Lagemaat, J. Revisiting the valence and conduction band size dependence of PbS quantum dot thin films. ACS Nano 2016, 10(3), 3302-3311.

[51] Xiao, Q.; Xia, B.; Liu, P. L.; Yang, Y.; Yang, G. Y.; Liu, J.; Lu, S. C.; Zhao, X. Z.; Ge, C. Y.; Chen, D.; Yang, J. R.; Liang, G. J.; Li, K. H.; Lan, X. Z.; Xiao, Z. W.; Zhang, J. B.; Gao, L. and Tang, J. In-situ surface patch-passivation via phosphorus oxygen bond for efficient PbS colloidal quantum dot infrared solar cells. Sol. Energy Mater. Sol. Cells 2022, 248, 112040.

Electronic Supplementary Material

High-performance quantum dots enabled by supplementary passivation using ethoxydiphenylphosphine

Hao Luo[1], Zhijiao Huang[1], Bo-Yi Deng[1], Chenyu Zhang[1], Yang Liu[1], Ke Peng[2], Rui Long[1], Xiangzhen Deng[1], Daoli Zhang[1], Liang Gao[3], Yanwei Wen[2], Jianbing Zhang[1] ✉, and Jiang Tang[3]

[1] *School of Integrated Circuits, Huazhong University of Science and Technology, Wuhan 430074, China*
[2] *School of Materials Science and Engineering, Huazhong University of Science and Technology, Wuhan 430074, China*
[3] *Wuhan National Laboratory for Optoelectronics, Huazhong University of Science and Technology, Wuhan 430074, China*

✉ Address correspondence to jbzhang@hust.edu.cn

Supporting information to https://doi.org/10.26599/NR.2026.94908748

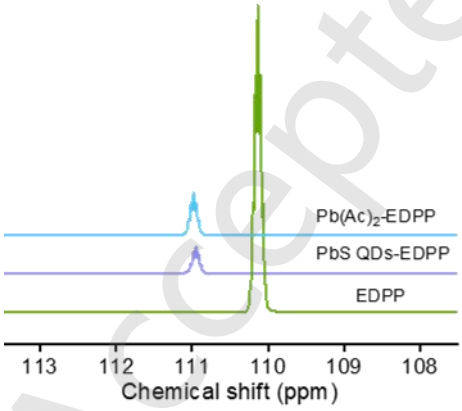

Figure S1 ^{31}P NMR spectra of EDPP, EDPP-treated PbS QDs, and EDPP mixed with Pb $(OAc)_2$

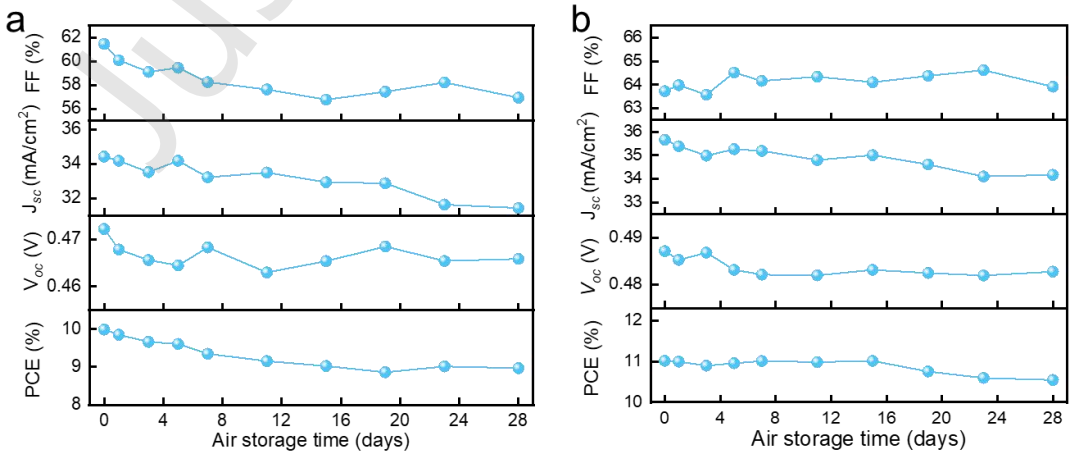

Figure S2 Stability of the (a) control and (b) EDPP-passivated solar cell under ambient air storage.

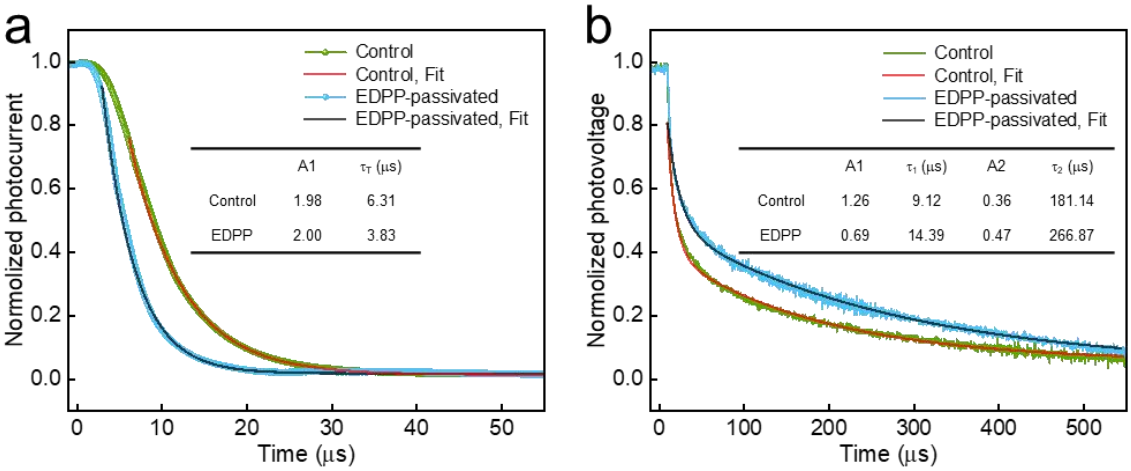

Figure S3 (a) Normalized transient photocurrent decay curves and (b) normalized transient photovoltage decay curves for the Control and EDPP-passivated solar cell.

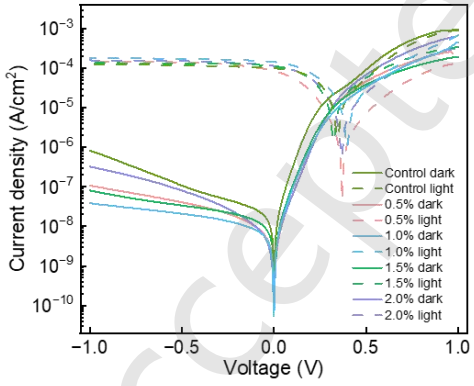

Figure S4 J-V curves of PbS photodetectors subjected to supplementary passivation with different concentrations of EDPP. The EDPP concentration is given as the volume percentage relative to DMF.

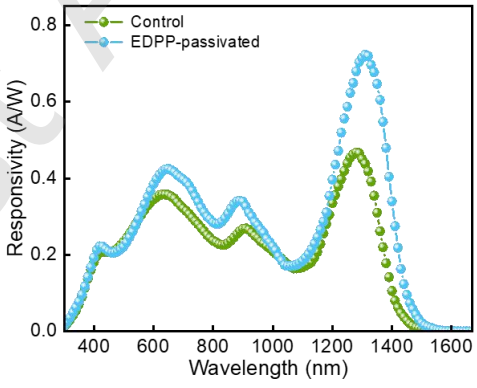

Figure S5 Spectral responsivity curves of the control and EDPP photodetectors.

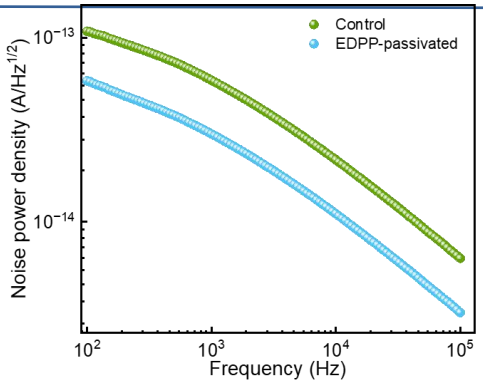

Figure S6 Noise power density of the control and EDPP photodetectors.

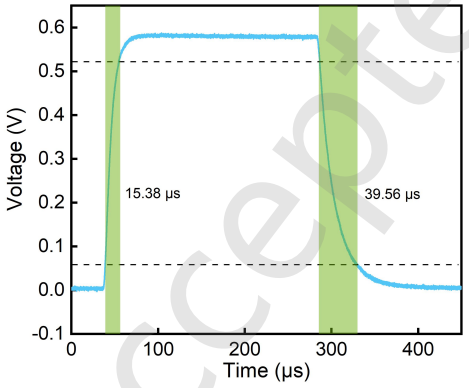

Figure S7 Response time of the control photodetectors.

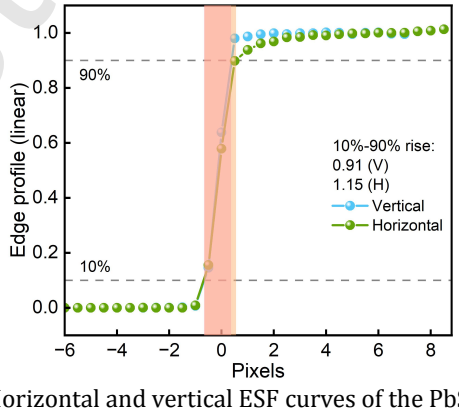

Figure S8 Horizontal and vertical ESF curves of the PbS QD imager.

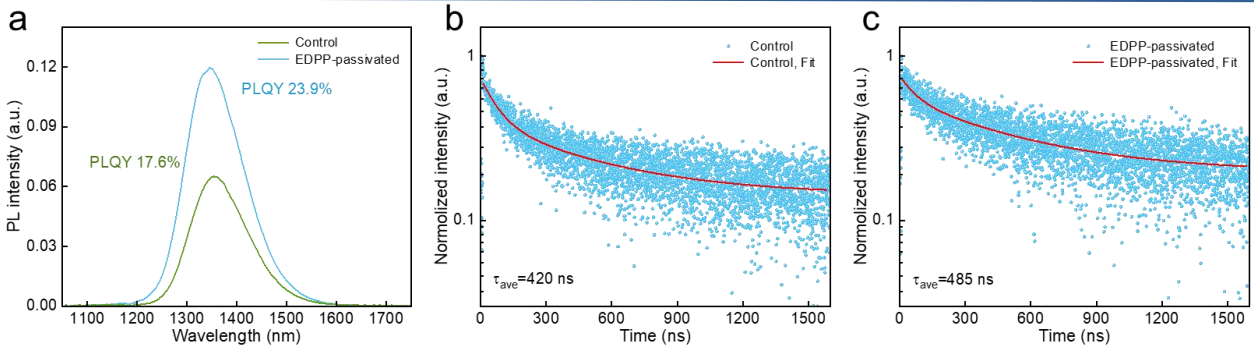

Figure S9 (a) PL spectra of oleic acid-passivated PbS QDs without and with EDPP treatment, and PL decay curves of oleic acid-passivated PbS QDs (b) before and (c) after EDPP treatment.

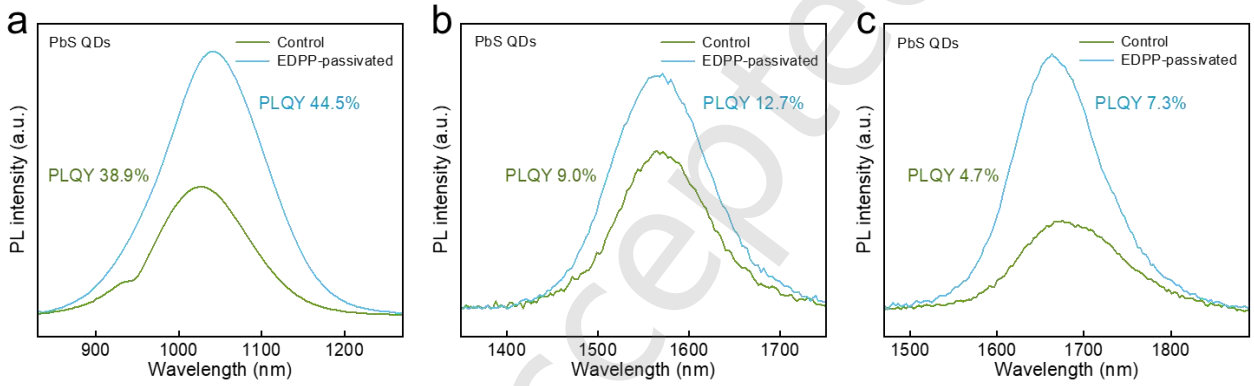

Figure S10 PL spectra of oleic acid-passivated PbS QDs with first excitonic absorption peaks at (a) 900 nm, (b) 1550 nm, and (c) 1650 nm, measured without and with EDPP treatment.

Table S1 Elemental compositions of control and EDPP-passivated films

Film	Pb (%)	S (%)	Br (%)	I (%)	P (%)
Control	45.2	42.5	2.8	9.5	0
EDPP-passivated	44.0	43.7	2.3	8.9	1.1

Table S2 The performance PbS QDs based solar cells w/o and w/ EDPP.

Device	Solar illumination	V_{OC} (V)	J_{SC} (mA/cm^2)	FF (%)	PCE (%)

Control	AM 1.5G	0.472	34.47	61.44	9.99
	1100nm filter	0.399	4.73	62.24	1.21
EDPP	AM 1.5G	0.485	35.61	63.70	11.01
	1100nm filter	0.420	5.52	64.68	1.50

Table S3 Comparison of the quantum dots infrared solar cells.

Year	QDs with exciton peak	IR-V_{oc} (V)	IR-J_{sc} (mA/cm^2)	IR-FF (%)	IR-PCE (%)	Ref
2018	1350 nm PbS	0.32	3.44	61	0.67	[1]
2018	1200 nm PbS	0.39	3.84	65	0.99	[2]
2018	1250 nm PbS	0.41	4.10	64	1.10	[3]
2018	1250 nm PbS	0.38	3.88	65	0.96	[4]
2019	1188 nm PbS	0.43	5.60	56	1.34	[5]
2019	1771 nm PbS	0.23	5.50	56	0.71	[6]
2020	1305 nm PbS	0.43	4.30	64	1.10	[7]
2021	PbSe-1088 nm/PbS	0.35	6.38	55	1.24	[8]
2021	1295 nm PbSe	0.35	6.78	54	1.31	[9]
2022	1305 nm PbS	0.44	4.81	64	1.36	[10]
2022	1275 nm PbS	0.42	4.78	61	1.23	[11]
2022	1550 nm PbS	0.29	8.66	47	1.18	[12]
2023	1270 nm PbS	0.39	5.56	59	1.30	[13]
2024	1270 nm PbSe	0.29	6.36	57	1.04	[14]
2024	1246 nm PbS	0.45	4.22	67	1.27	[15]
2024	1250 nm PbS	0.43	5.50	66	1.37	[16]
	1310 nm PbS	0.42	5.52	65	1.50	This work

Table S4 PLQY and enhancement performance of different QD systems before and after EDPP treatment.

QD systens	original PLQY	PLQY after EDPP treatment	absolute enhancement value	relative enhancement rate
InP/ZnSe/ZnS	94%	98%	4%	4.3%
CdSe/ZnS	96%	99%	3%	3.1%

CdSe	11.8%	17.7%	5.9%	50.0%
PbS/CdS	25.6%	29.2%	3.6%	14.1%
PbSe	9.1%	12.8%	3.7%	40.7%
PbSe/PbS	11.4%	15.2%	3.8%	33.3%
900 nm PbS	38.9%	44.5%	5.6%	14.4%
1310 nm PbS	17.6%	23.9%	6.3%	35.8%
1550 nm PbS	9.0%	12.7%	3.7%	41.1%
1650 nm PbS	4.7%	7.3%	2.6%	55.3%

Reference

[1] Bi, Y.; Pradhan, S.; Gupta, S.; Akgul, M. Z.; Stavrinadis, A. and Konstantatos, G. Infrared solution‐processed quantum dot solar cells reaching external quantum efficiency of 80% at 1.35 μm and Jsc in excess of 34 mA cm-2. Adv. Mater. 2018, 30(7), 1704928

[2] Choi, J.; Jo, J. W.; de Arquer, F. P. G.; Zhao, Y. B.; Sun, B.; Kim, J.; Choi, M. J.; Baek, S. W.; Proppe, A. H.; Seifitokaldani, A.; Nam, D. H.; Li, P.; Ouellette, O.; Kim, Y.; Voznyy, O.; Hoogland, S.; Kelley, S. O.; Lu, Z. H. and Sargent, E. H. Activated electron‐transport layers for infrared quantum dot optoelectronics. Adv. Mater. 2018, 30(29), 1801720

[3] Kim, J.; Ouellette, O.; Voznyy, O.; Wei, M.; Choi, J.; Choi, M. J.; Jo, J. W.; Baek, S. W.; Fan, J.; Saidaminov, M. I.; Sun, B.; Li, P.; Nam, D. H.; Hoogland, S.; Lu, Z. H.; García de Arquer, F. P. and Sargent, E. H. Butylamine‐catalyzed synthesis of nanocrystal inks enables efficient infrared CQD solar cells. Adv. Mater. 2018, 30(45), 1803830.

[4] Baek, S. W.; Ouellette, O.; Jo, J. W.; Choi, J.; Seo, K. W.; Kim, J.; Sun, B.; Lee, S. H.; Choi, M. J.; Nam, D. H.; Quan, L. N.; Kang, J.; Hoogland, S.; García de Arquer, F. P.; Lee, J. Y. and Sargent, E. H. Infrared cavity-enhanced colloidal quantum dot photovoltaics employing asymmetric multilayer electrodes. ACS Energy Lett. 2018, 3(12), 2908-2913.

[5] Baek, S. W.; Molet, P.; Choi, M. J.; Biondi, M.; Ouellette, O.; Fan, J.; Hoogland, S.; García de Arquer, F. P.; Mihi, A. and Sargent, E. H. Nanostructured back reflectors for efficient colloidal quantum‐dot infrared optoelectronics. Adv. Mater. 2019, 31(33), 1901745.

[6] Bi, Y.; Bertran, A.; Gupta, S.; Ramiro, I.; Pradhan, S.; Christodoulou, S.; Majji, S. N.; Akgul, M. Z. and Konstantatos, G. Solution processed infrared- and thermo-photovoltaics based on 0.7 eV bandgap PbS colloidal quantum dots. Nanoscale 2019, 11(3), 838-843.

[7] Xia, Y.; Liu, S. S.; Wang, K.; Yang, X. K.; Lian, L. Y.; Zhang, Z. M.; He, J. G.; Liang, G. J.; Wang, S.; Tan, M. L.; Song, H. S.; Zhang, D. L.; Gao, J. B.; Tang, J.; Beard, M. C. and Zhang, J. B. Cation‐exchange synthesis of highly monodisperse PbS quantum dots from ZnS nanorods for efficient infrared solar cells. Adv. Funct. Mater. 2019, 30(4), 1907379.

[8] Liu, S. S.; Zhang, C. J.; Li, S. Y.; Xia, Y.; Wang, K.; Xiong, K.; Tang, H. D.; Lian, L. Y.; Liu, X. X.; Li, M. Y.; Tan, M. L.; Gao, L.; Niu, G. D.; Liu, H.; Song, H. S.; Zhang, D. L.; Gao, J. B.; Lan, X. Z.; Wang, K.; Sun, X. W.; Yang, Y.; Tang, J. and Zhang, J. B. Efficient infrared solar cells employing quantum dot solids with strong inter‐dot coupling and efficient passivation. Adv. Funct. Mater. 2020, 31(9), 2006864.

[9] Liu, S. S.; Xiong, K.; Wang, K.; Liang, G. J.; Li, M. Y.; Tang, H.; Yang, X. K.; Huang, Z.; Lian, L. Y.; Tan, M. L.; Wang, K.; Gao, L.; Song, H. S.; Zhang, D. L.; Gao, J. B.; Lan, X. Z.; Tang, J. and Zhang, J. B. Efficiently passivated PbSe quantum dot solids for infrared photovoltaics. ACS Nano 2021, 15(2), 3376-3386.

[10] Xiao, Q.; Xia, B.; Liu, P. L.; Yang, Y.; Yang, G. Y.; Liu, J.; Lu, S. C.; Zhao, X. Z.; Ge, C. Y.; Chen, D.; Yang, J. R.; Liang, G. J.; Li, K. H.; Lan, X. Z.; Xiao, Z. W.; Zhang, J. B.; Gao, L. and Tang, J. In-situ surface patch-passivation via phosphorus oxygen bond for efficient PbS colloidal quantum dot infrared solar cells. Sol. Energy Mater. Sol. Cells 2022, 248, 112040.

[11] Li, M. Y.; Chen, S. W.; Zhao, X. Z.; Xiong, K.; Wang, B.; Shah, U. A.; Gao, L.; Lan, X. Z.; Zhang, J. B.; Hsu, H. Y.; Tang, J. and Song, H. S. Matching charge extraction contact for infrared PbS colloidal quantum dot solar cells. Small 2021, 18(1), 2105495.

[12] Wang, H. B.; Nakao, S.; Miyashita, N.; Oteki, Y.; Giteau, M.; Okada, Y.; Takamoto, T.; Saito, H.; Magaino, S.; Takagi, K.; Hasegawa, T.; Kubo, T.; Kinoshita, T.; Nakazaki, J. and Segawa, H. Spectral splitting solar cells constructed with InGaP/GaAs two-junction subcells and infrared PbS quantum dot/ZnO nanowire subcells. ACS Energy Lett. 2022, 7(8), 2477-2485.

[13] Liu, S. S.; Li, M. Y.; Xiong, K.; Gao, J. B.; Lan, X. Z.; Zhang, D. L.; Gao, L.; Zhang, J. B. and Tang, J. Efficient quantum dot infrared solar cells with enhanced low-energy photon conversion via optical engineering. Nano Res. 2022, 16(2), 2392-2398.

[14] Liu, S. S.; Wang, M.; Yu, X.; Li, H.; Lu, H. F.; Wen, X. Y.; Li, M. Y. and Zhang, J. B. Efficient PbSe quantum dot infrared photovoltaic applying MXene modified ZnO electron transport layer. Adv. Opt. Mater. 2023, 12(1), 2301252.

[15] Liu, S. S.; Deng, C. J.; Wang, M.; Wei, A. S.; Luo, T. Y.; Lu, H. F.; Wen, X. Y.; Li, M. Y. and Zhang, J. B. Efficient quantum dot infrared photovoltaic with enhanced charge extraction via applying gradient electron transport layers. Adv. Opt. Mater. 2024, 12(17), 2303256.

[16] Wang, M.; Liu, S. S.; Wei, A. S.; Luo, T. Y.; Wen, X. Y.; Li, M. Y. and Lu, H. F. Effective charge collection of electron transport layers for high-performance quantum dot infrared solar cells. ACS Appl. Mater. Interfaces 2024, 16(19), 24572-24579.